IEICE TRANS. COMMUN., VOL.E96–B, NO.7 JULY 2013

PAPER

Accurate Imaging Method for Moving Target with Arbitrary Shape for Multi-Static UWB Radar

Ryo YAMAGUCHI[†a)], ***Student Member***, **Shouhei KIDERA**[†], ***and*** **Tetsuo KIRIMOTO**[†], ***Members***

SUMMARY Ultra-wideband pulse radar is a promising technology for the imaging sensors of rescue robots operating in disaster scenarios, where optical sensors are not applicable because of thick smog or high-density gas. For the above application, while one promising ultra-wideband radar imaging algorithm for a target with arbitrary motion has already been proposed with a compact observation model, it is based on an ellipsoidal approximation of the target boundary, and is difficult to apply to complex target shapes. To tackle the above problem, this paper proposes a non-parametric and robust imaging algorithm for a target with arbitrary motion including rotation and translation being observed by multi-static radar, which is based on the matching of target boundary points obtained by the range points migration (RPM) algorithm extended to the multi-static radar model. To enhance the imaging accuracy in situations having lower signal-to-noise ratios, the proposed method also adopts an integration scheme for the obtained range points, the antenna location part of which is correctly compensated for the estimated target motion. Results from numerical simulations show that the proposed method accurately extracts the surface of a moving target, and estimates the motion of the target, without any target or motion model.

key words: *UWB pulse radar, moving target, range points migration (RPM), non-parametric imaging, multi-static UWB radar*

1. Introduction

Ultra-wideband (UWB) pulse radar has immeasurable potential for the near-field imaging sensors of rescue robots, as it has high range resolution in scenes where optical sensors are hardly applicable, such as fire scenes with heavy smoke, scenes of nebulous gas and scenes having strong backlight. Targeting these applications, various imaging algorithms for UWB radar systems have been developed in recent decades, most of which are based on data synthesis; e.g., synthetic aperture radar (SAR) [1], time-reversal algorithms [2], [3], and range migration methods [4], [5]. However, each method has a unique drawback such as an impractically large computational burden, particularly for three-dimensional problems, or the spatial resolution and accuracy being strictly limited by the signal bandwidth and wavelength, and thus being insufficient to identify the detailed structure of a target shape. By contrast, the recently established imaging algorithm SEABED (Shape Estimation Algorithm based on Boundary scattering transform and Extraction of Directly scattered waves) accomplishes fast non-parametric imaging using reversible transforms between the observed range and target boundary [6]. However, this method has a negative side, inasmuch as the imaging accuracy is readily degraded when applying the derivative operation to obtained range points, and it also requires a process to connect range points, and is thus not suitable for noisy cases or situations of rich interference resulting from objects having complicated shapes. As a solution to this difficulty, the range points migration (RPM) algorithm has been proposed [7]; the algorithm is based on group mapping from observed range points to target boundary points and retains sufficient accuracy even for a complicated target boundary or in noisy situations by avoiding the task of connecting observed range points or a derivative operation. However, the above algorithms [6] and [7] assume a static target, despite the imaging of a moving target such as a human being an indispensable task in a disaster scene and other scenarios.

Although there have been many articles on the detection and localization of moving targets for radar systems mainly focusing on far-field measurement [8], [9], the imaging accuracy of these methods should be degraded in the near-field case because the scattering center moves on the target boundary according to dynamical change of the observation angle in the case of a non-point target. To be suitable to the near field model, a method [10] in which the model fitting approximates a local shape of a target as part of an ellipse with distances measured with a small number of antennas has been proposed. Although this algorithm works well for several types of target shapes that are similar to an ellipse, it was confirmed that the imaging accuracy is seriously degraded in the case of non-elliptical shapes.

To free radar systems from the above limitations, this paper adopts the RPM method as a non-parametric imaging approach, where the multi-static extension is introduced so that the approach is suitable for moving target estimation and a sufficient number of target points are obtained. In addition, the target motion is estimated using target point matching for adjacent observation times. A notable feature of this method is that it is possible to estimate both the target shape and motion without using any approximation model. In addition, this method has the distinct advantage that the final image reconstruction is more robust through application of the RPM to the integrated set of range points for all observation times, where the equivalent antenna locations are correctly compensated with the estimated target motion. The results obtained from numerical simulations, including those for noisy situations, verify the effectiveness of the proposed method from quantitative and statistical points of view.

Manuscript received January 29, 2013.

[†]The authors are with the Graduate School of Informatics and Engineering, The University of Electro-Communications, Chofu-shi, 182-8585 Japan.

a) E-mail: yamaguchi@secure.ee.uec.ac.jp

DOI: 10.1587/transcom.E96.B.2014

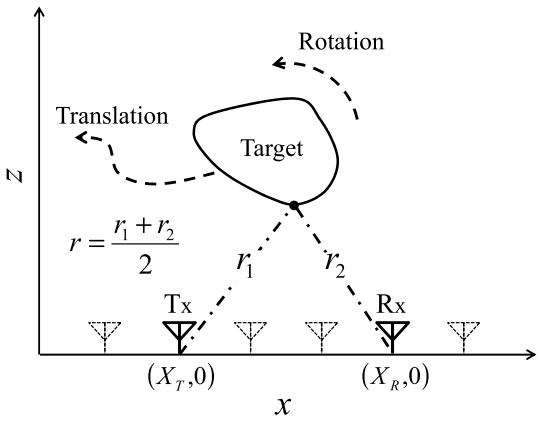

Fig. 1 System model.

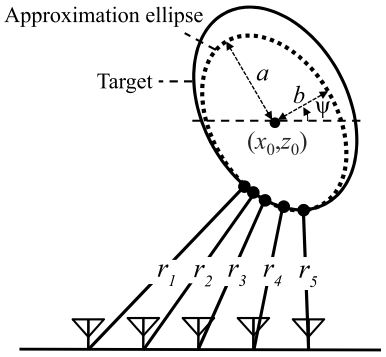

Fig. 2 Conventional scheme for ellipse fitting.

This paper is organized as follows. In Sect. 2, the system model assuming multi-static observation is presented. Section 3 describes the conventional method for moving target imaging and points out its limitation. The basic idea and the detailed methodology of the proposed method are described in Sect. 4. Section 5 presents the numerical simulation results of imaging and motion estimation for each method, and quantitative analysis is also provided. Concluding remarks are given in Sect. 6.

2. System Model

The system model is shown in Fig. 1. This paper deals with the two-dimensional problem and the transverse electric (TE) mode wave for simplicity. It assumes that the target has arbitrary shape with a clear boundary and moves with arbitrary motion including rotation and translation. A number (greater than two) of omni-directional antennas are arranged along the x-axis at fixed intervals to form a multi-static radar configuration. The transmitting signal is a mono-cycle pulse, whose central wavelength is denoted λ and its fractional bandwidth defined in [11] is about 100%. Here, it is assumed that observation data are acquired instantaneously and the target motion during the data acquisition interval is negligible. The n-th observation time is defined as $t_n = n\Delta t$ ($1 \le n \le N$), where Δt denotes the interval of the observation event. The locations of the transmitting and receiving antennas are defined as $\boldsymbol{L}_\mathrm{T} = (X_\mathrm{T}, 0)$ and $\boldsymbol{L}_\mathrm{R} = (X_\mathrm{R}, 0)$, respectively. For each combination of $\boldsymbol{L}_\mathrm{T}$ and $\boldsymbol{L}_\mathrm{R}$, the output of the Wiener filter is denoted $s(\boldsymbol{q}')$, where $\boldsymbol{q}' = (\boldsymbol{L}_\mathrm{T}, \boldsymbol{L}_\mathrm{R}, r')^T$ is defined with $r' = \mathrm{c}\tau/2$, delay time τ and speed of the radio wave c. $\boldsymbol{q} = (\boldsymbol{L}_\mathrm{T}, \boldsymbol{L}_\mathrm{R}, r)^T$ is the range point, which is extracted from the local maxima of $s(\boldsymbol{q}')$ as to r', where r denotes the extracted range. This procedure is summarized in [7].

3. Conventional Method

As the conventional imaging scheme for a moving target in near-field measurement, a traditional method [10] is introduced here for performance comparison. This section briefly explains its methodology and states the problem of this method as follows. First, the conventional method employs five antennas, each of which takes a role of monostatic radar, and then determines a target boundary at each observation time using an observed range, and tracks the target motion by approximating part of the target shape as an ellipse. Figure 2 is a fundamental illustration of the conventional method. Here, $\boldsymbol{P} = (a, b, x_0, z_0, \psi)$ denotes the parameters of an ellipse whose major axis is a, minor axis is b, and center is (x_0, z_0), and the angle from the x-axis to the minor axis is denoted ψ in the counter-clockwise direction. Specifically, the ellipse with parameters $\boldsymbol{P}$ is expressed as

$$\left(\frac{\cos^2\psi}{a^2}+\frac{\sin^2\psi}{b^2}\right)(x-x_0)^2+\left(\frac{\sin^2\psi}{a^2}+\frac{\cos^2\psi}{b^2}\right)(z-z_0)^2 +\sin 2\psi\left(\frac{1}{a^2}-\frac{1}{b^2}\right)(x-x_0)(z-z_0)=1. \quad (1)$$

Here, $\boldsymbol{P}^{(n)}$ for the ellipse at t_n is estimated as

$$\boldsymbol{P}^{(n)} = \arg\min_{\boldsymbol{P}} \sum_{i=1}^{N_\mathrm{a}} \left| r_i^{(n)} - r_i(\boldsymbol{P}) \right|^2, \quad (2)$$

where N_a denotes the number of antennas, $r_i^{(n)}$ denotes the range observed at the i-th antenna at t_n, and $r_i(\boldsymbol{P})$ denotes the minimum distance between the i-th antenna position $\boldsymbol{x}_i$ and the boundary points of $\boldsymbol{P}$. This method accurately reconstructs a target and its motion in the case of a shape well approximated by an ellipse, with a small number of antennas. However, since a target boundary is locally approximated as an ellipse, the imaging accuracy is severely degraded in the case of a target boundary far from an elliptical shape.

4. Proposed Method

4.1 RPM Extended to Multi-Static Radar

As a solution for the above problem, this paper adopts the matching scheme for obtained target points along adjacent observation times. As a notable difference from the conventional method [10], the matching scheme employs multi-static radar and adopts the RPM method extended to this model for target image creation. This is because the multi-static observation can remarkably increase the number of

independent target boundary points, as has been verified for the multi-static SEABED method [12]. Since we adopt the target points matching scheme for the motion estimation, the number of target points directly affects the accuracy. In addition, for a mono-static model, we need to scan the transmitting and receiving antenna mechanically with highly accurate position control. This generally requires a longer data acquisition time compared with the multi-static model, where much faster electrical switching of the RF signal can be achieved by a semiconductor switch. This is the motivation for extending the multi-static model.

The original RPM assumes a mono-static model, and the target boundary is determined by the accurate direction of arrival (DOA) estimation scheme, which exploits the global feature of the range point map. By avoiding the procedure of a range derivative or connection, RPM achieves accurate and robust imaging even in situation of severe interference or noise. It is expected that this property can be held in the multi-static observation. The extension of RPM to the multi-static model is introduced as follows. Multi-static RPM is based on the simple principle that a target boundary point should exist on an ellipse formulated as $\sqrt{(x-X_{\mathrm{T}})^2+z^2}+\sqrt{(x-X_{\mathrm{R}})^2+z^2}=2r$. Thus, each target point (x,z) can be calculated from the corresponding angle of arrival θ. Figure 3 shows the relationship between the intersection points of the ellipses and the angle of arrival. Here, the i-th range point obtained in the n-th observation is defined as $\boldsymbol{q}_i^{(n)}=\left(\boldsymbol{L}_{\mathrm{T},i}^{(n)},\boldsymbol{L}_{\mathrm{R},i}^{(n)},r_i^{(n)}\right)^T\left(i=1,\cdots,M_{\mathrm{q}}^{(n)}\right)$, where $\boldsymbol{L}_{\mathrm{T},i}^{(n)}$ and $\boldsymbol{L}_{\mathrm{R},i}^{(n)}$ denote the i-th locations of transmitting and receiving antenna in n-th observation, $r_i^{(n)}$ denotes the i-th observed range in n-th observation and $M_{\mathrm{q}}^{(n)}$ denotes the total number of range points at n-th observation. The optimum θ for $\boldsymbol{q}_i^{(n)}$ is calculated as

$$\theta_{\mathrm{opt}}\left(\boldsymbol{q}_i^{(n)}\right)=\underset{0\le\theta\le\pi}{\arg\max}\sum_{\boldsymbol{q}_j^{(n)}\in Q}s\left(\boldsymbol{q}_j^{(n)}\right)\exp\left[-\frac{\left\{\theta-\theta\left(\boldsymbol{q}_i^{(n)},\boldsymbol{q}_j^{(n)}\right)\right\}^2}{2\sigma_\theta^2}\right]\times\exp\left[-\frac{D\left(\boldsymbol{q}_i^{(n)},\boldsymbol{q}_j^{(n)}\right)^2}{2\sigma_D^2}\right],\tag{3}$$

where Q denotes a set of obtained range points, and

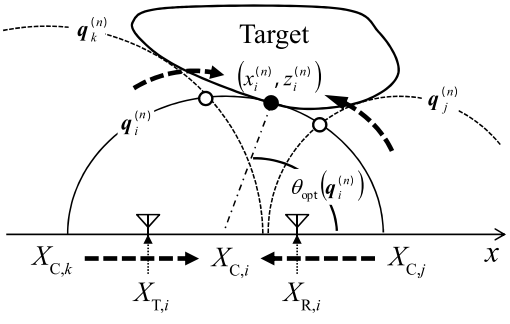

Fig. 3 Relationship between the target boundary and the convergence orbit of the intersection points at n-th observation.

$\theta\left(\boldsymbol{q}_i^{(n)},\boldsymbol{q}_j^{(n)}\right)$ denotes the angle from the x-axis to the line connecting the point $X_{\mathrm{C},i}=\left(X_{\mathrm{T},i}^{(n)}+X_{\mathrm{R},i}^{(n)}\right)/2$ and the point of intersection of the two ellipses determined by $\boldsymbol{q}_i^{(n)}$ and $\boldsymbol{q}_j^{(n)}$. σ_θ and σ_D are empirically determined as similar values in [7], and $D\left(\boldsymbol{q}_i^{(n)},\boldsymbol{q}_j^{(n)}\right)$ is defined as

$$D\left(\boldsymbol{q}_i^{(n)},\boldsymbol{q}_j^{(n)}\right)=\min\left(\left\|\boldsymbol{L}_{\mathrm{T},i}^{(n)}-\boldsymbol{L}_{\mathrm{T},j}^{(n)}\right\|^2+\left\|\boldsymbol{L}_{\mathrm{R},i}^{(n)}-\boldsymbol{L}_{\mathrm{R},j}^{(n)}\right\|^2,\left\|\boldsymbol{L}_{\mathrm{T},i}^{(n)}-\boldsymbol{L}_{\mathrm{R},j}^{(n)}\right\|^2+\left\|\boldsymbol{L}_{\mathrm{R},i}^{(n)}-\boldsymbol{L}_{\mathrm{T},j}^{(n)}\right\|^2\right).\tag{4}$$

The location of the estimated target point $\boldsymbol{p}_i^{(n)}=\left(x_i^{(n)},z_i^{(n)}\right)$ at the n-th observation is determined as

$$\left.\begin{array}{l}x_i^{(n)}=X_{\mathrm{C},i}+a_i\cos\theta_{\mathrm{opt}}\left(\boldsymbol{q}_i^{(n)}\right)\\ z_i^{(n)}=b_i\sin\theta_{\mathrm{opt}}\left(\boldsymbol{q}_i^{(n)}\right)\end{array}\right\},\left(i=1,\cdots,M_{\mathrm{p}}^{(n)}\right),\tag{5}$$

where $a_i=r_i^{(n)}$, $b_i=\sqrt{{r_i^{(n)}}^2-\left(X_{\mathrm{T},i}^{(n)}-X_{\mathrm{C},i}^{(n)}\right)^2}$, and $M_{\mathrm{p}}^{(n)}$ denotes the number of target points at the n-th observation time. Here, the false target points resulting from noisy components can be removed by assessing the evaluation value in the right term of Eq. (3), which is similar to the procedure for Eq. (18) in [7]. Then, in most cases, $M_q^{(n)}\neq M_p^{(n)}$ holds. In addition, this method is easily extended to the arbitrary alignment of array antennas and not limited to linear alignment along the x-axis, because it only assesses the degree of accumulation of intersection points of ellipses. This expansion is needed in the final image reconstruction using range points at all observation times, which is detailed in Sect. 4.3. This imaging method accomplishes non-parametric and accurate imaging even in the situation that the range point map has a complicated distribution, because it can estimate an accurate DOA by not only using the local distribution of range points, but also exploiting their global feature in Eq. (3).

4.2 Motion Estimation

We now consider the motion estimation using the target points obtained with the multi-static RPM method. Here, the locations of target points at t_n are denoted $\boldsymbol{p}_j^{(n)}\left(j=1,\cdots,M_{\mathrm{p}}^{(n)}\right)$. The target point after rotation and translation of $\boldsymbol{p}_i^{(n-1)}$ is expressed by

$$\tilde{\boldsymbol{p}}_i^{(n)}(\boldsymbol{R},\boldsymbol{T})=\boldsymbol{R}\left(\boldsymbol{p}_i^{(n-1)}-\boldsymbol{C}^{(n-1)}\right)+\boldsymbol{C}^{(n-1)}+\boldsymbol{T},\tag{6}$$

where $\boldsymbol{R}$ denotes the rotation matrix, $\boldsymbol{T}$ denotes the translation motion vector and $\boldsymbol{C}^{(n-1)}$ denotes the barycentric position of target points calculated with a set $\boldsymbol{p}_i^{(n-1)}$. For motion estimation, the cost function is

$$F^{(n)}(\boldsymbol{R},\boldsymbol{T})=\sum_{i=1}^{M_{\mathrm{p}}^{(n-1)}}\min_j\left\|\boldsymbol{p}_j^{(n)}-\tilde{\boldsymbol{p}}_i^{(n)}(\boldsymbol{R},\boldsymbol{T})\right\|^2.\tag{7}$$

Figure 4 shows the spatial relationship between $\boldsymbol{p}_j^{(n)}$ and $\tilde{\boldsymbol{p}}_i^{(n)}(\boldsymbol{R},\boldsymbol{T})$. This method determines the target motion $\boldsymbol{R}^{(n)}$ and $\boldsymbol{T}^{(n)}$ from t_{n-1} to t_n as

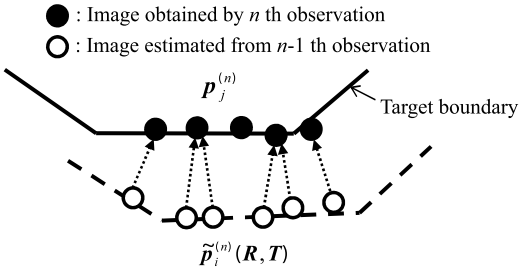

Fig. 4 Relationship between $\boldsymbol{p}_j^{(n)}$ and $\tilde{\boldsymbol{p}}_i^{(n)}(\boldsymbol{R},\boldsymbol{T})$ in Eq. (7).

$$\left(\boldsymbol{R}^{(n)},\boldsymbol{T}^{(n)}\right)=\underset{(\boldsymbol{R},\boldsymbol{T})}{\arg\min}\,F^{(n)}(\boldsymbol{R},\boldsymbol{T})\,. \tag{8}$$

4.3 Image Compensation with Target Motion

The final step of the proposed method reconstructs a target image by applying multi-static RPM to the range points, where the antenna location part of each range point is correctly compensated by the estimated target motion described in Sect. 4.2. This procedure is necessary to enhance the robustness against range fluctuations caused by random noise or interference, because the accuracy of the RPM method becomes more robust when employing a greater number of accurately extracted range points. This procedure is summarized as follows. Here, $\boldsymbol{q}_{\mathrm{C},i}^{(k,n)}$ denotes the compensated range points for the k-th observation event from $\boldsymbol{q}_i^{(n)}$. First, $n=1$ is set, and we move on to the following process.

Step 1). Set $k=n$, namely $\boldsymbol{q}_{\mathrm{C},i}^{(n,n)}=\boldsymbol{q}_i^{(n)}$ is set.

Step 2). Using target motion $\boldsymbol{R}^{(k)}$ and $\boldsymbol{T}^{(k)}$, $\boldsymbol{q}_{\mathrm{C},i}^{(k+1,n)}$ is compensated as

$$\boldsymbol{q}_{\mathrm{C},i}^{(k+1,n)}=\begin{pmatrix}\boldsymbol{R}^{(k+1)}&0&0\\0&\boldsymbol{R}^{(k+1)}&0\\0&0&1\end{pmatrix}\left[\boldsymbol{q}_{\mathrm{C},i}^{(k,n)}-\begin{pmatrix}\boldsymbol{C}^{(k)}\\\boldsymbol{C}^{(k)}\\0\end{pmatrix}\right]+\begin{pmatrix}\boldsymbol{C}^{(k)}\\\boldsymbol{C}^{(k)}\\0\end{pmatrix}+\begin{pmatrix}\boldsymbol{T}^{(k+1)}\\\boldsymbol{T}^{(k+1)}\\0\end{pmatrix}. \tag{9}$$

Step 3). If $k<N-1$ holds, set $k\leftarrow k+1$ and return to Step 2); otherwise go to Step 4) with $\boldsymbol{q}_{\mathrm{C,i}}^{(N,n)}$.

Step 4). The set of compensated range points at the n-th observation is defined as set $Q_{\mathrm{C}}^{(n)}=\bigcup_i \boldsymbol{q}_{\mathrm{C},i}^{(N,n)}$. If $n<N-1$ holds, set $n=n+1$ and return to Step 1); otherwise set $Q_{\mathrm{C}}^{(N)}=\bigcup_i \boldsymbol{q}_i^{(N)}$ and go to Step 5).

Step 5). Set $Q_{\mathrm{C}}=\bigcup_n Q_{\mathrm{C}}^{(n)}$ and produce target points by multi-static RPM using Q_{C} instead of Q in Eq. (3).

Figure 5 illustrates the relationship between the antenna locations of $\boldsymbol{q}_i^{(n)}$ and those of $\boldsymbol{q}_{\mathrm{C,i}}^{(N,n)}$ compensated from the n-th observation event to the N-th observation event. The figure shows that the target-moving model is equivalent to the antenna-moving model for the target at rest at the location of t_N. This indicates that the spatial resolution or accuracy

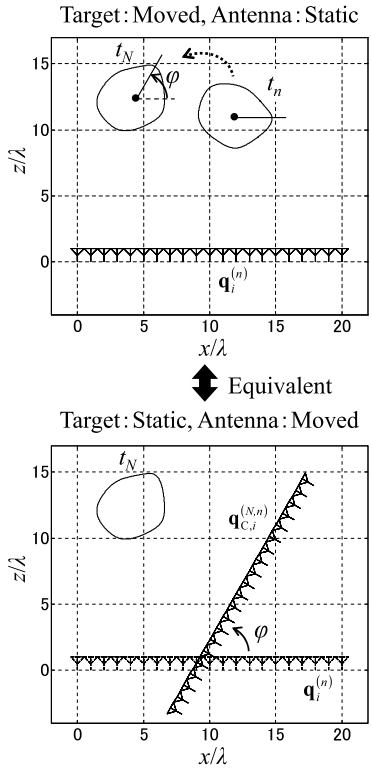

Fig. 5 Relationship between the antenna locations of $\boldsymbol{q}_i^{(n)}$ and those of $\boldsymbol{q}_{\mathrm{C,i}}^{(N,n)}$ compensated from the n-th to the N-th observation event.

of imaging can be enhanced by combining the range points over all observation events.

4.4 Procedure for the Proposed Method

The procedure for the proposed method is summarized as follows. First, $n=1$ is set.

Step 1). A set of target points $\boldsymbol{p}_j^{(n)}\left(j=1,\cdots,M_{\mathrm{p}}^{(n)}\right)$ is obtained by applying multi-static RPM to the observed range points $\boldsymbol{q}_j^{(n)}$ described in Sect. 4.1.

Step 2). If $n\geq 2$ holds, go to Step 3); otherwise set $n=n+1$ and return to Step 1).

Step 3). The target motion $\boldsymbol{R}^{(n)}$ and $\boldsymbol{T}^{(n)}$ are estimated using $\boldsymbol{p}_i^{(n-1)}\left(i=1,\cdots,M_{\mathrm{p}}^{(n-1)}\right)$ and $\boldsymbol{p}_j^{(n)}\left(j=1,\cdots,M_{\mathrm{p}}^{(n)}\right)$ described in Sect. 4.2.

Step 4). If $n=N$ holds, go to Step 5); otherwise set $n=n+1$ and return to Step 1).

Step 5). A final target image is reconstructed by applying multi-static RPM to the set of integrated range points as Q_{C}, the antenna location part of which are compensated by the estimated target motion, as described in Sect. 4.3.

Step 6). To suppress false images caused by random noise, remove the target points that satisfy

$$\zeta\left(\boldsymbol{q}_{\mathrm{C},i}^{(N,n)}\right)\leq\beta\max_{\boldsymbol{q}_{\mathrm{C},i}^{(N,n)}\in Q_{\mathrm{C}}}\zeta\left(\boldsymbol{q}_{\mathrm{C},i}^{(N,n)}\right) \tag{10}$$

where $\zeta\left(\boldsymbol{q}_{\mathrm{C},i}^{(N,n)}\right)$ denotes the maximum value of the right

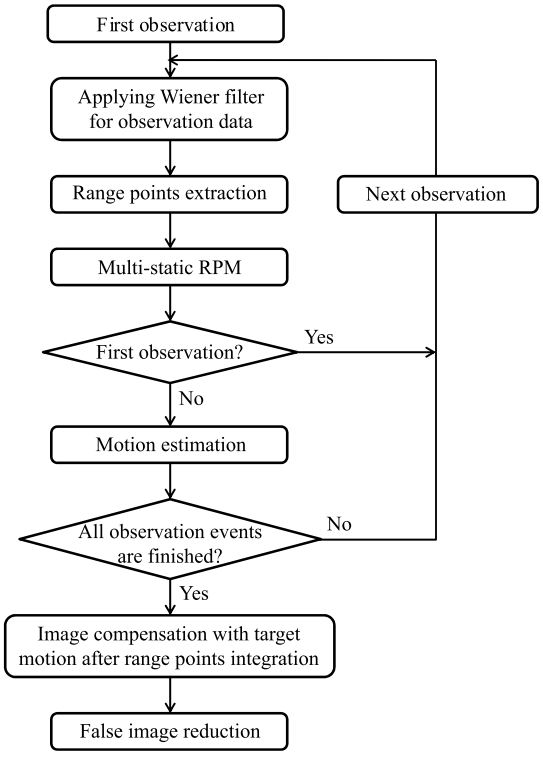

Fig. 6 Flowchart of the proposed method.

term in Eq. (3) and β is empirically determined.

Figure 6 is a flowchart of the proposed method.

5. Performance Evaluation in Numerical Simulations

5.1 Evaluation in Ideal Observation Model

This section investigates the performance of the conventional and proposed methods through numerical simulations. The target shape is assumed as in Fig. 1. The motion of barycentric point $(x_{\mathrm{G}}^{(n)}, z_{\mathrm{G}}^{(n)})$ of the target at the n-th observation time is set as

$$\left.\begin{aligned} x_{\mathrm{G}}^{(n)} &= x_0 + v_x t_n \\ z_{\mathrm{G}}^{(n)} &= z_0 + v_z \sin(\omega t_n) \end{aligned}\right\}, (n = 1, \cdots, N), \tag{11}$$

and the angle of target rotation is set as

$$\phi^{(n)} = \phi_0 \cos(\omega t_n), (n = 1, \cdots, N), \tag{12}$$

where $(x_0, z_0) = (16.0\lambda, 12.5\lambda)$, $v_x = -0.60\lambda/\Delta t$, $v_z = -1.50\lambda/\Delta t$, $\omega = 2\pi/\{(N-1)\Delta t\}$, $N = 21$ and $\phi_0 = 0.66$ rad. It is assumed that the target maintains the same posture relative to the direction of translation motion; e.g., in the case of human walking motion. Here, the received data are calculated by the geometric optics approximation, which is also used in [13], so as to assess the far field observation. While this type of data generation does not consider multiple scattering effects and frequency dependency of scattering phenomena, as reported in [14], we assume in this case only a single target being of size sufficiently larger than the wavelength or having no edge, where the frequency dependency of scattering is negligible. First, the performance of the conventional method is investigated. Figure 7 shows each ellipse estimated at each observation time using Eq. (2). Here, five transmitting and receiving antennas are located at $0.0\lambda \le x \le 20.0\lambda$ at intervals of 5.0λ, with each antenna playing the role of mono-static radar. This method requires a numerical calculation time of around 20 sec at each observation time for image and motion estimation when using a Xeon 2.4 GHz processor. Each estimated ellipse cannot correctly express the whole shape of a target because the ellipse approximation is totally inappropriate in this target case. The accuracy of the estimated motion of target is thus naturally degraded. For fair comparison with the proposed method, Fig. 8 shows each ellipse estimated by the conventional method using multi-static observation. To comply with the assumption presented in Sect. 2, the data acquisition times during the target moving is negligible, only 3 transmitting antennas are located at $(0.0\lambda, 0.0\lambda)$, $(10.0\lambda, 0.0\lambda)$ and $(20.0\lambda, 0.0\lambda)$, and 21 receiving antennas are located at $0.0\lambda \le x \le 20.0\lambda$ at intervals of λ. This is because in multi-receiving systems, the total acquisition time depends mainly on the amount of switching time for

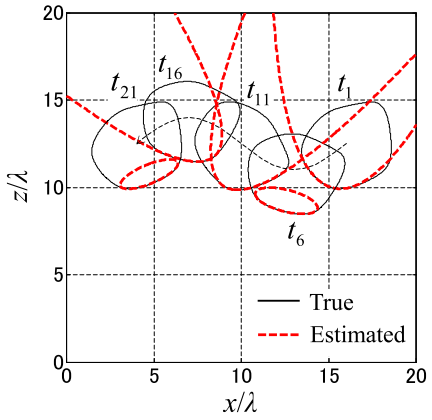

Fig. 7 Estimated ellipses by the conventional method with mono-static observation in noiseless situation at t_1, t_6, t_{11}, t_{16} and t_{21}.

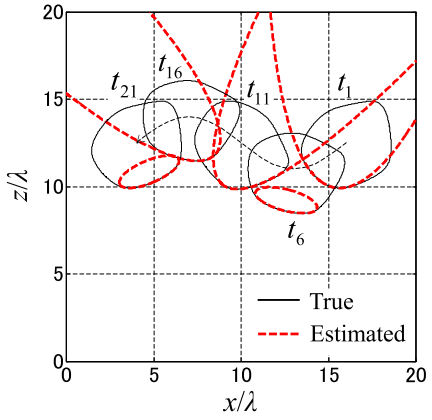

Fig. 8 Estimated ellipses by the conventional method with multi-static observation in noiseless situation at t_1, t_6, t_{11}, t_{16} and t_{21}.

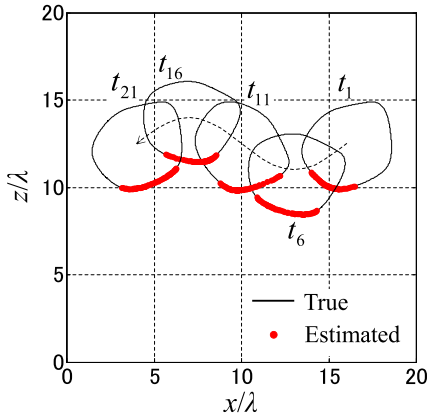

Fig. 9 Target boundary points obtained by multi-static RPM algorithm in noiseless situation at t_1, t_6, t_{11}, t_{16} and t_{21}.

the transmitting antennas. More detailed discussions about this point are described in the final paragraph of this section. This figure also indicates that even if multi-static observation is introduced, this problem is not essentially resolved because it employs the elliptical object model.

In contrast, Fig. 9 shows the target boundary points obtained by multi-static RPM at each observation time. $\sigma_\theta = \pi/75$ and $\sigma_D = 1.0\lambda$ are set. Here, for a fair comparison, the same observation model assumed in Fig. 8 is used, namely, 3 transmitting antennas and 21 receiving antennas. The multi-static RPM provides an accurate image regardless of the observation event. Figure 10 shows the estimated target motion obtained using the proposed method, where the vertical axis of (a)–(c) denote a difference value from prior observation time of the rotation angle, the translation value for x-axis and z-axis, respectively. Here, the simulated annealing algorithm [15] is employed to obtain a global optimum in Eq. (8), where the Levenberg-Marquardt method is sequentially used for local optimization. These figures show that the estimated motion including rotation and translation is accurately tracked by the proposed method even in the case of a non-elliptical target. That is, the proposed method has a non-parametric property in motion estimation for arbitrary target shape, which is a notable advantage over the conventional method [10]. The estimation error of the target motion is mainly ascribed to the degradation of the positioning accuracy of target points by RPM. Figure 11 shows the final target shape reconstructed with the range point integration described in Sect. 4.3, where each range point is correctly compensated by the estimated target motion. $\beta = 0.3$ is set. This result also demonstrates that the proposed method has been successful in accurately expanding the image area of the target boundary. Figure 12 shows the equivalent model of the antenna moving around the target at rest at position t_N, which is generated by the estimated target motion through range point integration. As shown in Fig. 12, the equivalent observation region (antenna locations) is significantly expanded, which enhances the imaging accuracy according to the RPM feature. In this case, the proposed method requires a numerical calculation time of around 21 sec when using

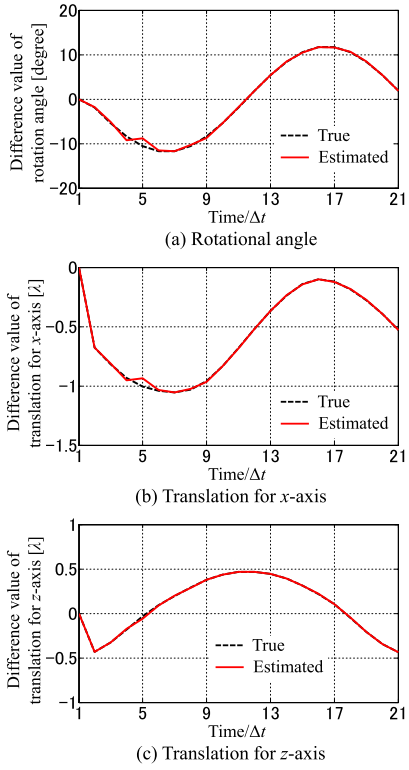

Fig. 10 Target motion for each observation time estimated by the proposed method in noiseless situation. ((a) Difference value of rotation angle (b) Difference value of translation motion for x-axis (c) Difference value of translation motion for z-axis.)

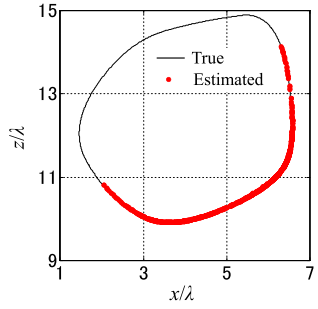

Fig. 11 Reconstructed target image by the proposed method with the range points integration as in Sect. 4.3 in noiseless situation.

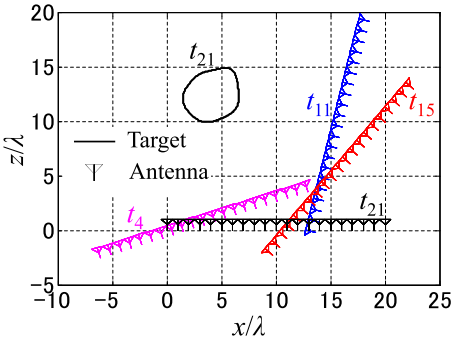

Fig. 12 The compensated locations of antenna from t_4, t_{11}, t_{15}, and when the target is assumed to be static at the position of t_{21}.

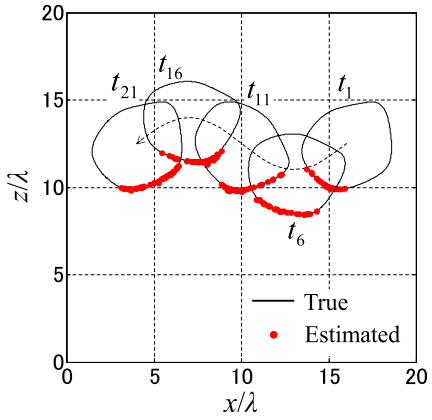

Fig. 13 Target boundary points obtained by multi-static RPM algorithm in S/N = 20 dB at t_1, t_6, t_{11}, t_{16} and t_{21}.

a Xeon 2.4 GHz processor for imaging and motion estimation in each observation interval Δt. This calculation time is dominated by the simulated annealing process in optimizing Eq. (8) to avoid a local optimum. While it is difficult to achieve real time estimation using our method in its present form, it might be possible to solve this difficulty by reducing the number of trials of simulated annealing, where the appropriate initial value of motion estimation is determined by the result in the prior observation. This type of modification should be considered in our future work for practical use.

Next, an example of a noisy situation is investigated. Gaussian white noise is added to the received signals. Here, the signal-to-noise ratio S/N is defined as the ratio of the peak instantaneous signal power to average noise power after applying a matched filter. Figure 13 shows the target boundary points obtained by multi-static RPM in each observation event at S/N = 20 dB. The figure verifies that multi-static RPM retains sufficient accuracy even in a noisy situation, while there are a small number of false images near the actual boundary. Figure 14 shows the target motions estimated by the proposed method in this case. The figure demonstrates that the motion tracking accuracy is worse than that in the noiseless situation owing to the target positioning errors occurred in RPM imaging. As a final image comparison, Figs. 15 and 16 show the reconstructed image compensated by estimated target motion without and with range point integration, respectively. In Fig. 15, the final image is directly compensated by the target motion with the RPM image in each observation event. Since the range points are not integrated, this image retains some fluctuations from the actual boundary. In contrast, Fig. 16 demonstrates that range point integration is effective in suppressing the accuracy degradation of the image seen in Fig. 13.

For quantitative evaluation of the imaging accuracy, $\epsilon(\boldsymbol{x}_{\mathrm{e}}^i)$ is introduced as

$$\epsilon\left(\boldsymbol{x}_{\mathrm{e}}^i\right) = \min_{x} \left\|\boldsymbol{x} - \boldsymbol{x}_{\mathrm{e}}^i\right\|, \ (i = 1, 2, \cdots, N_{\mathrm{T}}), \tag{13}$$

where $\boldsymbol{x}$ and $\boldsymbol{x}_{\mathrm{e}}^i$ express the locations of the true target points

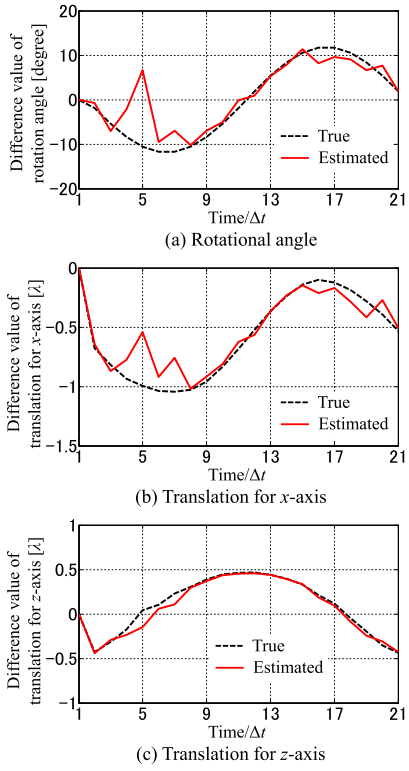

Fig. 14 Target motion for each observation time estimated by the proposed method in S/N = 20 dB. ((a) Difference value of rotation angle (b) Difference value of translation motion for x-axis (c) Difference value of translation motion for z-axis.)

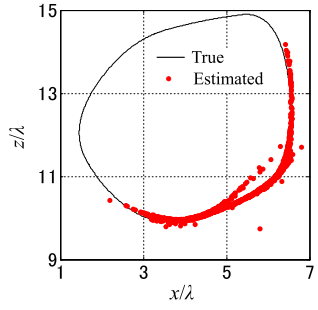

Fig. 15 Reconstructed target image by the proposed method without the range points integration as in Sect. 4.3 in S/N = 20 dB.

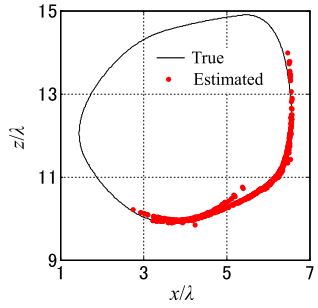

Fig. 16 Reconstructed target image by the proposed method including the range points integration as in Sect. 4.3 in S/N = 20 dB.

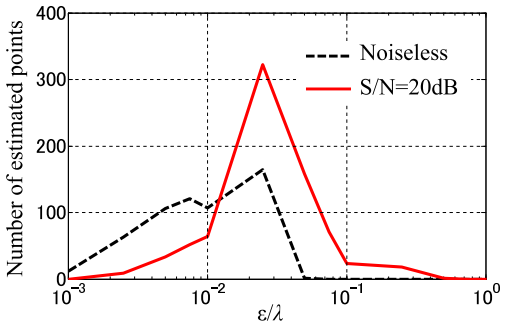

Fig. 17 Number of the estimated target points in noiseless situation and S/N = 20 dB.

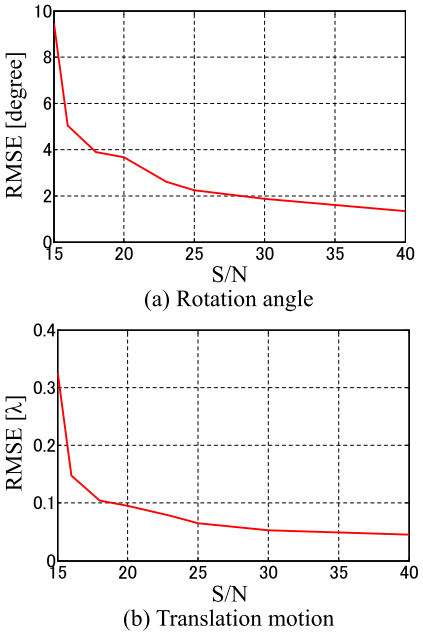

Fig. 18 Each RMSE versus S/N for the proposed method. (a) Rotation angle (b) Translation motion.

and the estimated points of the final image reconstructed with the proposed method, respectively. N_T is the total number of $\boldsymbol{x}_e^i$. Figure 17 plots the number of estimated points for each value of ϵ. N_T for each result is 685 in the noiseless situation, and 752 for S/N = 20 dB. This result indicates that the proposed method achieves imaging accuracy finer than 1 λ for all target points, even in the noisy situation. The root mean square error (RMSE) of ϵ is $9.4 \times 10^{-3}\lambda$ in the noiseless situation and 0.065λ when S/N = 20 dB.

For quantitative analysis from a statistical viewpoint, Fig. 18 illustrates the relationship between the RMSE in target motion and S/N for the proposed method, where figure (a), (b) show the rotation angle and translation motion versus S/N, respectively. Here, at each S/N value, the number of Monte-Carlo trials is set to 50, and each RMSE is the average for this number of trials. Figures 18(a) and (b) show that the proposed method retains accurate motion estimation, particularly for S/N $\geq$ 20 dB. Figure 19 illustrates the relationship between the RMSE in final target shape and S/N

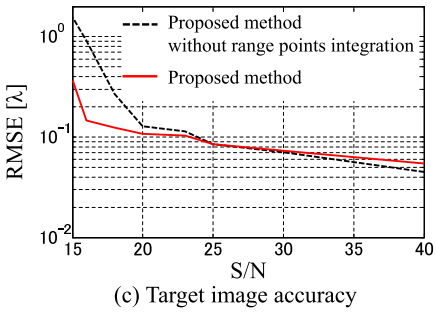

Fig. 19 RMSE in target imaging accuracy versus S/N for the proposed method.

for the proposed method. The figure indicates that the range point integration process of the proposed method enhances the imaging accuracy considerably S/N $\leq$ 20 dB.

5.2 Applicability to Realistic Situation

This section describes the applicability of our proposed method to realistic scenarios. The numerical simulations assumed in Sect. 5 correspond approximately to actual cases, when we assume a UWB mono-cycle signal with center wavelength λ = 6 cm (center frequency is 5 GHz) in considering the actual human body sizes (around 30 cm diameter). The observation time interval Δt should then be set at around 25 msec considering that the average speed of a human body is around 1.5 m/sec in this case. In addition, this simulation assumes that the target motion during the data acquisition interval is negligible, as described in Sect. 2. However, even if this condition is not strictly satisfied, namely, using the actually available measurement tools, the proposed method holds a sufficient accuracy to reconstruct the target image. First, some switching devices such as semiconductor switches can achieve switching times of about 0.1 msec; note that only switching of the transmitting signal is needed when using a multiple channel receiver. Second, the pulse repetition frequency in this case can be set above 50 MHz (maximum observation range is 6 m). Even if we perform coherent averaging on the receiver side about 1000 times, the data acquisition time for each antenna combination is estimated to be within 0.02 msec. Thus, the entire data acquisition process including signal switching and coherent averaging can be achieved within 0.26 msec using the observation model assumed in this simulation (3 transmitting and 21 receiving antennas). In this case, the target motion amount during data acquisition is estimated to be within 1mm (around 0.02 λ), and has a negligible effect on reconstructing the target shape with sufficient accuracy, whose size is around 5 λ diameter.

Here, to demonstrate the above discussion, the simulation in considering the target motion during data acquisition is investigated as follows. Figure 20 shows the target motions estimated by the proposed method considering the target motion during data acquisition time determined by the above scenario at noiseless situation. Figure 21 illustrates

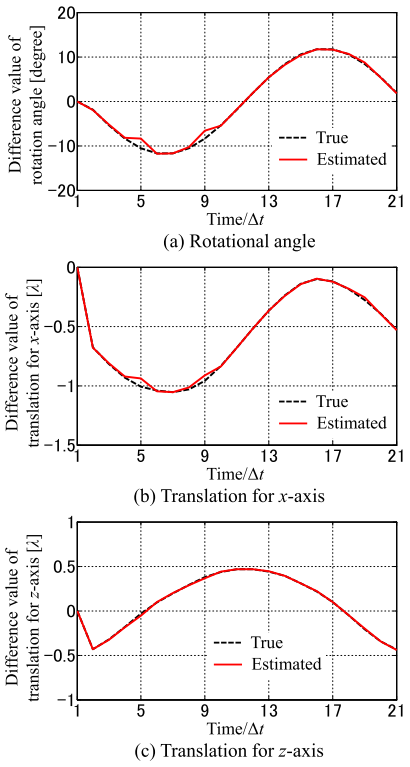

Fig. 20 Target motion for each observation time estimated by the proposed method in considering the target motion during data acquisition time. ((a) Difference value of rotation angle (b) Difference value of translation motion for x-axis (c) Difference value of translation motion for z-axis.)

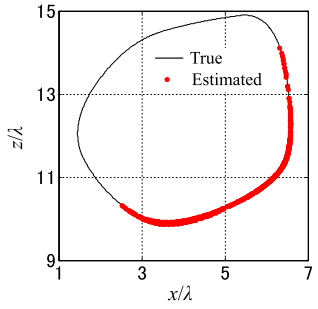

Fig. 21 Reconstructed target image by the proposed method including the range points integration as in Sect. 4.3 in considering the target motion during data acquisition time.

the final target shape reconstructed with the range point integration in this case. Figure 22 plots the number of estimated points for each value of ϵ with comparing the result obtained in not considering the target motion during data acquisition. These results verify that our proposed method maintains an sufficient accuracy for moving target imaging even in realistic situations. For the future work, we wish to establish a more complete method that can compensate an absolute estimation error caused by a target motion during data acquisition time.

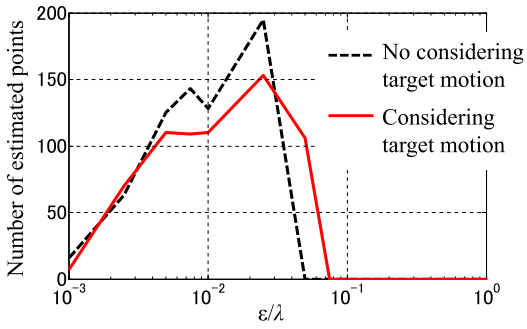

Fig. 22 Number of the estimated target points in no considering the target motion during data acquisition time and considering the target motion during data acquisition time.

6. Conclusion

This paper proposed a novel imaging method for a target with arbitrary shape and arbitrary motion including rotation and translation, which is based on the matching of target boundary points obtained by multi-static RPM for adjacent observation times. To enhance the accuracy and robustness of the final image reconstruction, this method also adopts range point integration, where the antenna locations are correctly compensated using the estimated target motion. Numerical simulations indicate that the conventional method based on an ellipse fitting scheme has an inevitable problem that the image fitting accuracy is severely degraded in the case of non-elliptical shapes because it is based on an ellipsoidal approximation of the target boundary and the motion estimation is naturally not informative in this case. In contrast, the proposed method offers a non-parametric imaging property guaranteed by the multi-static modeled RPM, and the target motion is accurately reproduced using the matching scheme for the obtained target points. Another feature of this method is that it is possible to enhance the robustness of final image reconstruction by incorporating range integration where the equivalent aperture size is remarkably expanded. Finally, numerical validation including the noisy case showed that the proposed method achieved extremely accurate motion estimation and target imaging on the order of $1/100$ of a wavelength.

Acknowledgment

This work is supported in part by the Grant-in-Aid for Scientific Research (B) (Grant No. 22360161) and the Grantin-Aid for Young Scientists (B) (Grant No. 23760364), promoted by Japan Society for the Promotion of Science (JSPS), and the Research Grant promoted by CASIO Science Promotion Foundation.

References

[1] D.L. Mensa, G. Heidbreder, and G. Wade, "Aperture synthesis by object rotation in coherent imaging," IEEE Trans. Nucl. Sci., vol.27, no.2, pp.989–998, April 1980.

[2] A.J. Devaney, "Time reversal imaging of obscured targets from multistatic data," IEEE Trans. Antennas Propag., vol.53, no.5, pp.1600–1610, May 2005.
[3] E.A. Marengo, F.K. Gruber, and F. Simonetti, "Time-reversal MUSIC imaging of extended targets," IEEE Trans. Image Process., vol.16, no.8, pp.1967–1984, Aug. 2007.
[4] J. Song, Q.H. Liu, P. Torrione, and L. Collins, "Two-dimensional and three dimensional NUFFT migration method for landmine detection using ground-penetrating radar," IEEE Trans. Geosci. Remote Sens., vol.44, no.6, pp.1462–1469, June 2006.
[5] F. Soldovieri, A. Brancaccio, G. Prisco, G. Leone, and R. Pieri, "A Kirchhoff-based shape reconstruction algorithm for the multimonostatic configuration: The realistic case of buried pipes," IEEE Trans. Geosci. Remote Sens., vol.46, no.10, pp.3031–3038, Oct. 2008.
[6] T. Sakamoto and T. Sato, "A target shape estimation algorithm for pulse radar systems based on boundary scattering transform," IEICE Trans. Commun., vol.E87-B, no.5, pp.1357–1365, May 2004.
[7] S. Kidera, T. Sakamoto, and T. Sato, "Accurate UWB radar 3-D imaging algorithm for complex boundary without wavefront connection," IEEE Trans. Geosci. Remote Sens., vol.48, no.4, pp.1993–2004, April 2010.
[8] J.R. Fienup, "Detecting moving targets in SAR imagery by focusing," IEEE Trans. Aerospace Electron. Syst., vol.37, no.3, pp.794–809, July 2001.
[9] A. Lin and H. Ling, "Doppler and direction-of-arrival (DDOA) radar for multiple-mover sensing," IEEE Trans. Aerosp. Electron. Syst., vol.43, no.4, pp.1496–1509, April 2007.
[10] T. Sakamoto and T. Sato, "Using a UWB radar imaging method with five antennas on a target with arbitrary translation and rotation motion," 5th European Conference on Antennas and Propagation (EuCAP), EUR Congressi, Rome, Italy, April 2011.
[11] Federal Communications Commission (FCC), Office of Engineering and Technology (OET) Bulletin no.65, Supplement C, p.35, Aug. 1997.
[12] S. Kidera, Y. Kani, T. Sakamoto, and T. Sato, "Fast and accurate 3-D imaging algorithm with linear array antennas for UWB pulse radars," IEICE Trans. Commun., vol.E91-B, no.8, pp.2683–2691, Aug. 2008.
[13] Y. Abe, S. Kidera, and T. Kirimoto, "Accurate image expansion method using range points based ellipse fitting for UWB imaging radar," IEICE Trans. Commun., vol.E95-B, no.7, pp.2424–2432, July 2012.
[14] S. Kidera, T. Sakamoto, and T. Sato, "A high-resolution imaging algorithm without derivatives based on waveform estimation for UWB pulse radars," IEICE Trans. Commun., vol.E90-B, no.6, pp.1487–1494, June 2007.
[15] S. Kirkpatrick, C.D. Gelatt, and M.P. Vecchi, "Optimization by simulated annealing," Science, no.220, pp.671–680, 1983.

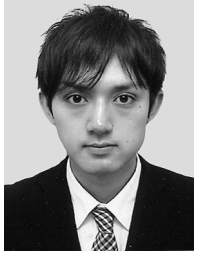

Ryo Yamaguchi received his B.E. degrees in Electronic Engineering from University of Electro-Communications in 2011. He is currently studying for an M.M degree at the Graduate School of Informatics and Engineering, University of Electro-Communications. His current research interest is advanced radar signal processing for UWB radar systems.

Shouhei Kidera received his B.E. degree in Electrical and Electronic Engineering from Kyoto University in 2003 and M.I. and Ph.D. degrees in Informatics from Kyoto University in 2005 and 2007, respectively. He is an assistant professor in Graduate School of Informatics and Engineering, University of Electro-Communications, Japan. His current research interest is in advanced signal processing for the near field radar, UWB radar. He is a member of the Institute of Electrical and Electronics Engineering (IEEE) and the Institute of Electrical Engineering of Japan (IEEJ).

Tetsuo Kirimoto received the B.S. and M.S. and Ph.D. degrees in Communication Engineering from Osaka University in 1976, 1978 and 1995, respectively. During 1978–2003 he stayed in Mitsubishi Electric Corp. to study radar signal processing. From 1982 to 1983, he stayed as a visiting scientist at the Remote Sensing Laboratory of the University of Kansas. From 2003 to 2007, he joined the University of Kitakyushu as a Professor. Since 2007, he has been with the University of Electro-Communications, where he is a Professor at the Graduate School of Informatics and Engineering. His current study interests include digital signal processing and its application to various sensor systems. Prof. Kirimoto is a senior member of IEEE and a member of SICE (The Society of Instrument and Control Engineers) of Japan.